Article

Unconventional bulk superconductivity in YFe2Ge2 single crystals

Chen, Jiasheng, Gamza, Monika, Banda, Jacintha, Murphy, Keiron, Tarrant, James, Brando, Manuel and Grosche, F. Malte

Chen, Jiasheng, Gamza, Monika ORCID: 0000-0003-3360-4006, Banda, Jacintha, Murphy, Keiron, Tarrant, James, Brando, Manuel and Grosche, F. Malte (2020) Unconventional bulk superconductivity in YFe2Ge2 single crystals. Physical Review Letters, 125 (237002). pp. 1-6. ISSN 0031-9007

Unconventional Bulk Superconductivity in YFe_2Ge_2 Single Crystals

Jiasheng Chen,[1,*] Monika B. Gamża,[2] Jacintha Banda,[3] Keiron Murphy,[1,†] James Tarrant,[1] Manuel Brando,[3] and F. Malte Grosche[1]

[1]Cavendish Laboratory, University of Cambridge, Cambridge CB3 0HE, United Kingdom
[2]Jeremiah Horrocks Institute for Mathematics, Physics and Astronomy, University of Central Lancashire, PR1 2HE Preston, United Kingdom
[3]Max Planck Institute for Chemical Physics of Solids, Nöthnitzer Straße 40, 01187 Dresden, Germany

(Received 28 July 2020; revised 17 September 2020; accepted 9 October 2020; published 30 November 2020)

Sharp superconducting transition anomalies observed in a new generation of single crystals establish that bulk superconductivity is intrinsic to high purity YFe_2Ge_2. Low temperature heat capacity measurements suggest a disorder and field dependent residual Sommerfeld coefficient, consistent with disorder-induced in-gap states as expected for a sign-changing order parameter. The sevenfold reduction in disorder scattering in these new crystals to residual resistivities $\simeq 0.45\ \mu\Omega\,\mathrm{cm}$ was achieved using a new liquid transport growth technique, paving the way for multiprobe experiments investigating the normal and superconducting states of YFe_2Ge_2.

DOI: 10.1103/PhysRevLett.125.237002

The iron-based layered compound YFe_2Ge_2 has been reported as a new unconventional superconductor [1], which differs from other iron-based superconductors [2] by its lack of group-V (pnictogen) or group-VI (chalcogen) elements and its more three dimensional Fermi surface geometry [3,4]. Nevertheless, YFe_2Ge_2 shares key properties of the alkali metal iron arsenides, $(K/Rb/Cs)Fe_2As_2$: (i) a similarly enhanced Sommerfeld coefficient, $C/T \sim 100\ \mathrm{mJ/mol\,K^2}$ [5–8]; (ii) bad metal behavior at room temperature, with resistivity ρ of order $200\ \mu\Omega\,\mathrm{cm}$ [9]; and (iii) a strong suppression of the superconducting transition temperature T_c by disorder scattering [10]. The highly correlated low temperature state and its crossover to incoherent bad metal behavior at high temperature [11–13] have been attributed to Hund's coupling, which forces the iron d electrons into a high spin state, causing significant quasiparticle mass enhancement independently of the shape of the Fermi surface [14]. Initially, no heat capacity anomalies were observed at the superconducting transition in polycrystals [15] or single crystals [16], casting doubt on the intrinsic nature of superconductivity in YFe_2Ge_2. Further, systematic improvements of polycrystal quality produced the first thermodynamic evidence of superconductivity in YFe_2Ge_2 [17], clarified the primary origin of crystalline imperfections in YFe_2Ge_2, and demonstrated that disorder rapidly suppresses the transition at a rate commensurate with expectations for a sign-changing order parameter [18]. This motivated renewed efforts to produce bulk superconducting single crystals, which are required for detailed experiments probing the strongly correlated normal state and the superconducting gap symmetry in YFe_2Ge_2.

Here, we report that improved YFe_2Ge_2 crystals display sharp signatures of the superconducting transition in heat capacity, magnetization, and resistivity, proving that superconductivity is indeed intrinsic to YFe_2Ge_2 of sufficient quality. We find that the size of the superconducting heat capacity anomaly and the extrapolated residual Sommerfeld ratio $\gamma_0 = \lim_{T\to 0} C/T$ correlate strongly with the disorder level and that γ_0 displays a further, distinct magnetic field dependence. Our findings are consistent with unconventional superconductivity with a sign-changing gap function. This advance is facilitated by modified flux growth techniques that produce YFe_2Ge_2 single crystals of superior quality, with residual resistivity $\rho_0 < 0.45\ \mu\Omega\,\mathrm{cm}$ and residual resistance ratio $\mathrm{RRR} \equiv \rho(300\ \mathrm{K})/\rho_0 \sim 430$, establishing horizontal liquid transport as a powerful method for producing ultrahigh quality crystals of challenging materials.

Methods.—Our crystal growth experiments are designed to enhance Fe occupancy on the Fe site, which in polycrystals proved to be the determining factor for achieving low disorder [18]. A comprehensive crystal growth study using the conventional Sn-flux method demonstrated that lowering the growth temperatures leads to higher quality [16]. This has motivated our approach, which reduces the temperature at which crystals precipitate from the melt by increasing the effective flux-to-charge ratio. Multiple batches of YFe_2Ge_2 single crystals have been grown with Sn-flux methods using (i) standard flux growth (SF) as described in [19] and used in previous crystal growth studies on YFe_2Ge_2 [5,16], (ii) modified flux growth (MF) from a polycrystalline YFe_2Ge_2 precursor with a reduced peak temperature between 850 and 1150 °C, or (iii) horizontal flux [or "liquid transport" (LT)] growth across a temperature gradient in a two-zone furnace with the cold end at 500 °C [20], a relatively little used technique that has

recently been put forward primarily for its higher crystal yield [26]. The advantages of LT and MF growth versus SF growth are discussed below. The in-plane electrical resistance was determined using a standard four-terminal ac technique in a Quantum Design Physical Properties Measurement System to < 0.4 K. Data were scaled to match the published resistivity of 190 $\mu\Omega\,$cm at 300 K [5]. Heat capacity measurements employed the pulse-relaxation method in a Quantum Design Physical Properties Measurement System to below 0.4 K and a compensated heat pulse method in a ^{3}He/^{4}He dilution fridge to 50 mK [27]. The magnetization data were taken in a Cryogenic SQUID magnetometer to below 0.45 K and were corrected for the effect of demagnetizing fields by approximating the sample shape as a rectangular prism. Powder XRD patterns were collected at room temperature in the Bragg–Brentano geometry with Cu $K\alpha$ radiation at 40 kV and 40 mA on a Bruker D8 diffractometer equipped with a Lynxeye XE detector to reduce the effects of Fe fluorescence and $K\beta$ radiation. Refinements of the powder patterns showed no evidence of secondary phases except for occasional Sn-flux inclusions. Lattice parameters were determined by referring to an internal Ge standard and using the Le Bail method.

Low-temperature heat capacity and electrical resistivity of YFe_2Ge_2 crystals from different growth batches are compared in Fig. 1. Crystals grown using standard flux methods have extrapolated $T = 0$ residual resistivity $\rho_0 \simeq 3.5\ \mu\Omega\,$cm, corresponding to RRR $\simeq$ 50–60. Some of these samples show resistive transitions, but none displays a superconducting heat capacity anomaly, confirming the findings of the previous single crystal study [16]. The modified flux growth from polycrystal precursors leads to a marked improvement, reaching $\rho_0 \simeq 1\ \mu\Omega\,$cm and RRR $\simeq$ 200 in the best batches. These samples show full resistive transitions, which often split into two steps, and they show broad heat capacity anomalies similar to those observed in the best polycrystals with similar RRR values [17,18]. Crystals grown in the liquid transport setup with a horizontal temperature gradient display the lowest residual resistivity $\rho_0 \simeq 0.45\ \mu\Omega\,$cm and reach resistance ratios of up to RRR $\simeq$ 430. These samples show sharp heat capacity jumps at a bulk T_c of about 1.1 K.

Resistive, thermodynamic, and magnetic signatures of the superconducting transition in YFe_2Ge_2 in MF and LT samples are compared in Fig. 2. An applied magnetic field of 2.5 T completely suppresses the superconducting heat capacity anomaly in both YFe_2Ge_2 samples [Figs. 2(c) and 2(d)], revealing the same underlying normal-state $C/T \approx 100\,\mathrm{mJ/mol\,K^2}$. The heat capacity jump $\Delta C(T_c)/T_c$ of $\sim$40% of the normal-state Sommerfeld coefficient $\gamma_n \simeq 100\ \mathrm{mJ/mol\,K^2}$ observed

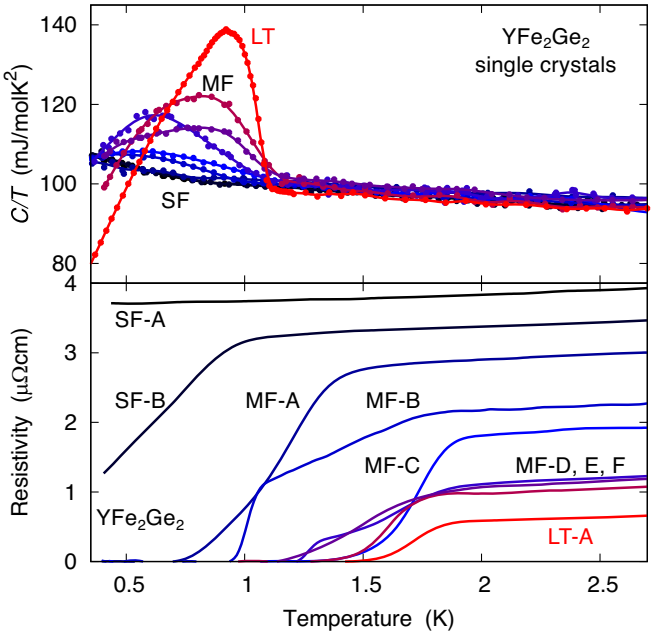

FIG. 1. Sommerfeld ratio of the heat capacity C/T (upper panel) and electrical resistivity (lower panel) of YFe_2Ge_2 single crystals from different growth batches. SF = standard flux growth, MF = modified flux growth, LT = liquid transport growth. These samples show a wide variation in their heat capacity superconducting anomaly, resistive transition, and residual resistivity. Lower residual resistivities correlate with sharper superconducting heat capacity anomalies.

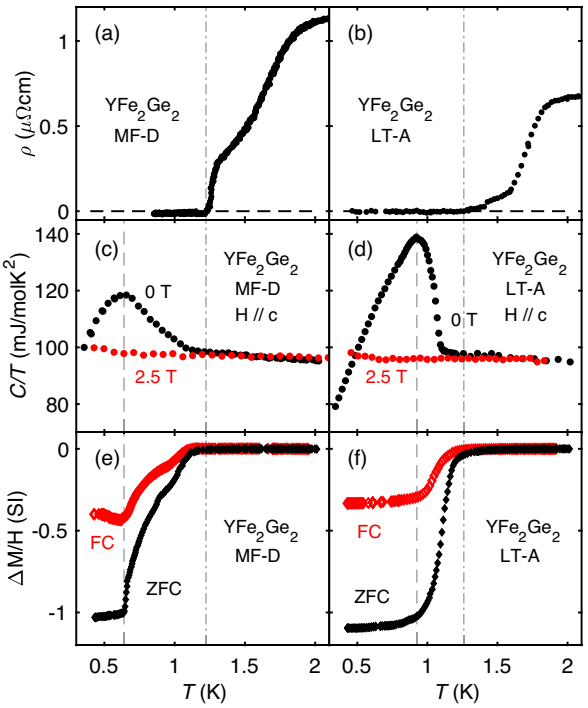

FIG. 2. Superconducting transition signatures for two high-quality batches of YFe_2Ge_2 samples. [(a),(b)] Electrical resistivity ρ, [(c),(d)] Sommerfeld coefficient of the heat capacity C/T, [(e),(f)] magnetization (FC = field cooled, ZFC = zero − field cooled). The vertical dash-dotted lines denote the temperatures at which resistivity drops to zero in (a) and (b). The vertical dashed lines indicate the peaks of C/T in (c) and (d).

in the highest quality batch LT-A [Figs. 2(d) and 3] falls well below $\Delta C(T_c)/T_c \approx 1.43\gamma_n$ expected in a conventional s-wave superconductor but is close to that observed in the isostructural compound KFe_2As_2 [6]. SQUID magnetometry provides further evidence of bulk superconductivity in samples with RRR $\gtrsim 150$. The zero-field-cooled diamagnetic response in Figs. 2(e) and 2(f) approaches 100% just below the peak of the specific heat transition for samples from batch MF-D and LT-A, respectively. The field-cooled diamagnetic screening is of order 30%, similar to or larger than values customarily found in other bulk superconducting type-II superconductors (e.g., [28]). Low temperature heat capacity measurements probe the superconducting state more closely (Fig. 3). Extrapolating the linear temperature dependence of C/T below 0.7 K to $T = 0$ yields a residual Sommerfeld ratio $\gamma_0 \approx 0.4\gamma_n$ at zero field, which rises further as the applied field is increased (inset to Fig. 3). The magnitude of γ_0/γ_n as well as its field dependence are similar to observations in some other iron-based superconductors (e.g., [29]). The diamagnetic screening and the sharp heat capacity jump at the transition both suggest 100% bulk superconductivity in the highest quality samples. This is consistent with the mean free path ℓ and the scattering rate τ^{-1} extracted from resistivity measurements, using the approach described in [18]: the residual resistivity $\rho_0 \simeq 0.45\ \mu\Omega\,\mathrm{cm}$ of LT-grown crystals translates to $\ell \simeq 2400$ Å, far larger than the coherence length $\xi \simeq 180$ Å [17], and to $\tau^{-1} \simeq 0.09\ \mathrm{meV}/\hbar$, well below the threshold of about 0.2 meV expected within the Abrikosov–Gorkov approach [18,30] from the bulk T_c. The suppressed jump height and residual Sommerfeld coefficient in heat capacity measurements could alternatively result from strong inhomogeneity of composition or disorder level, producing a large nonsuperconducting fraction [2]. Such a scenario is difficult to reconcile with the uniform and high RRR values of all LT crystals extracted from a given batch and with the sharp heat capacity jump, all of which would require a very specific inhomogeneity profile. Spectroscopic studies such as NMR or μSR will be needed to determine the superconducting volume fraction unambiguously.

We now consider the role of crystal growth methodology in producing high-quality crystals (Fig. 4). Structural refinement of XRD data confirms an observation previously made in polycrystals [18], namely that improved crystal quality correlates with increasing c-axis lattice parameters (Fig. 5). This is consistent with Fe deficiency on the Fe site presenting the dominant source of disorder. This interpretation is further supported by single-crystal XRD at 100 K, which identifies significant Ge substitution on the Fe site in the sample with the lowest RRR and c-axis lattice parameter (Batch SF-B) [20], whereas bulk superconducting samples showed no signs of Ge-Fe site disorder.

In standard flux growth, all elements are fully dissolved before crystals are formed on cooling. To achieve a high yield, this requires a low flux-to-charge ratio, which in turn leads to a high peak temperature, usually about 1200 °C, and a high precipitation temperature. The schematic phase diagram in Fig. 6 illustrates the benefits of our alternative

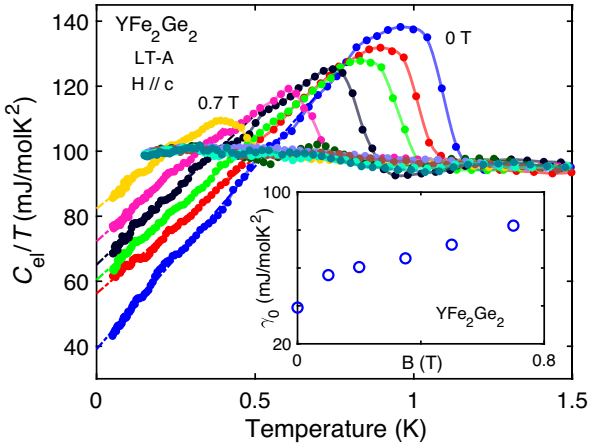

FIG. 3. Electronic contribution to the specific heat capacity versus temperature, C_{el}/T, of a YFe_2Ge_2 single crystal from batch LT-A. Applied fields are 0 T (labeled), 0.1 T (red), 0.2 T (green), 0.35 T (black), 0.5 T (pink), 0.7 T (labeled), and 1 T (dark green). C_{el} is obtained by subtracting from the total specific heat capacity the fitted nuclear contribution $C_n(H,T) = \alpha(H)/T^2$ [20]. Inset: extrapolated zero-temperature residual C_{el}/T versus applied field.

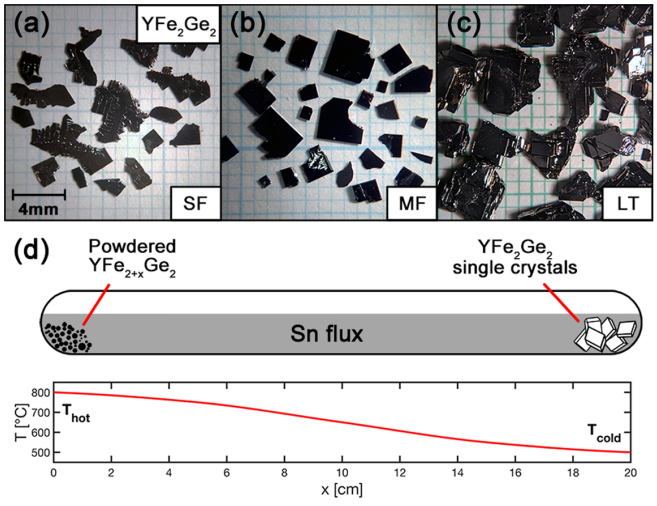

FIG. 4. YFe_2Ge_2 single crystals produced using (a) SF, (b) MF, and (c) LT methods on millimeter-scale paper. Dendrite formation is observed in the SF-grown crystals, which usually contain only one well defined facet along the [100] a axis in each crystal. Crystals from the MF batches display less obvious dendritic patterns, smoother surfaces, and more rectangular shapes. Both the SF- and MF-grown crystals form thin plates, whereas those from the LT batch are bulkier in the [001] c direction with thickness reaching up to 2 mm. (d) Schematic illustration of the LT technique.

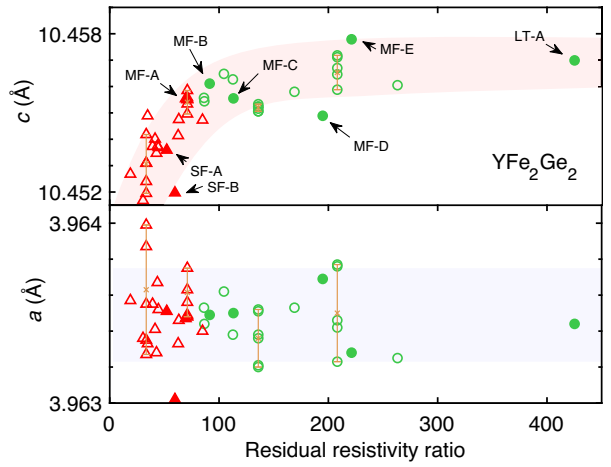

FIG. 5. Lattice constants c (upper panel) and a (lower panel) of polycrystalline (open symbols) [18] and single-crystal (solid symbols) YFe_2Ge_2 samples, as obtained by powder XRD refinement, versus the corresponding RRR values. Green circles (red triangles) indicate that superconducting heat capacity anomalies have (have not) been observed. Error bars are estimated from repeated measurements on selected batches of polycrystals. The pink and blue shades are guides to the eyes.

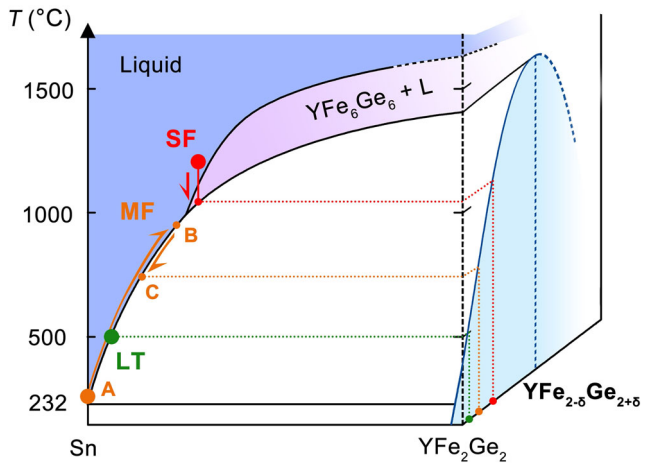

FIG. 6. Schematic phase diagram illustrating YFe_2Ge_2 growth from Sn flux. SF growth proceeds from fully molten charge (red trajectory) and leads to Fe-poor crystals if the apex of the $YFe_{2-x}Ge_{2+x}$ homogeneity range lies at an off-stoichiometric composition. MF growth proceeds from a saturated solution of YFe_2Ge_2 (orange trajectory), enabling a higher flux-to-charge ratio in the melt and consequently lower precipitation temperatures. It produces crystals with closer to the ideal stoichiometry but with considerable inhomogeneity. LT growth precipitates at a well-defined low temperature and produces the highest quality crystals. At temperatures above ~1000 °C (purple zone), alien phases such as YFe_6Ge_6 may form, which affects the composition of the melt.

growth protocols. We attribute the difficulties in growing high-quality YFe_2Ge_2 crystals by the SF method to (i) the formation of secondary phases such as YFe_6Ge_6 at $T > 1000$ °C, which affects the composition of the melt, and (ii) the position of the apex of the narrow YFe_2Ge_2 homogeneity range at a slightly off-stoichiometric composition $YFe_{2-\delta}Ge_{2+\delta}$, which favors Fe-poor crystals precipitating at high temperatures. In the modified flux method, the peak temperature can be reduced well below ~1000 °C, while maintaining stoichiometry in the melt thanks to the polycrystalline precursor. Because the precursor is not fully dissolved, the melt remains a saturated solution of YFe_2Ge_2 in Sn. The melt composition follows the liquidus curve from point A to point B as it heats up, gradually dissolving more of the charge. As the melt is cooled back down, it tracks the liquidus in reverse toward point C while precipitating $YFe_{2-\eta}Ge_{2+\eta}$ ($0 < \eta < \delta$). This process limits the crystal growth to the desired low temperature region of the liquidus in the complex quaternary phase diagram, avoiding the formation of secondary phases and facilitating the growth of crystals with a higher Fe:Ge ratio, closer to the stoichiometric composition. The heating and cooling cycle $C \rightarrow B \rightarrow C$ can be repeated to increase yield: every heating segment preferentially dissolves small crystallites on the polycrystalline charge, whereas each cooling segment preferentially deposits onto larger crystals forming elsewhere in the crucible. YFe_2Ge_2 is thereby gradually transported from the polycrystal precursor toward the single crystals, keeping the desired stoichiometry intact. Using Fe-rich precursors may further encourage high Fe content in the crystals. However, because precipitation occurs over a range of temperatures, the resulting crystals exhibit some inhomogeneity of composition and disorder level, causing broad resistive and heat capacity anomalies. Liquid transport growth extends the idea of using the flux to transport material from precursor toward crystals to a horizontal geometry. Maintaining a constant temperature at the cold end of the flux mixture ensures that crystal growth takes place at a fixed point on the liquidus. This improves homogeneity and reduces Fe-Ge site disorder, resulting in the sharpened bulk transition in crystals from Batch LT-A.

Liquid transport growth has produced a sevenfold reduction in disorder level in the new generation of YFe_2Ge_2 crystals, which, for the first time, show sharp thermodynamic transition anomalies indicative of bulk superconductivity. It thereby emerges as a powerful tool for growing ultrapure crystals of YFe_2Ge_2 and other challenging materials. Our findings mirror key results in iron arsenides such as $(Ba/K)Fe_2As_2$. The fast suppression of bulk superconductivity by lattice disorder excludes a conventional isotropic s-wave scenario. The small $\Delta C(T_c)/\gamma_n T_c$ can be ascribed to multigap superconductivity, as in KFe_2As_2 [6,31]. Likewise, the significant extrapolated residual Sommerfeld ratio γ_0 might point toward a further downturn in C_{el}/T at temperatures below the range of our current experiments if the gap on part of the Fermi surface is much smaller than $k_B T_c$. However, because γ_0 rises with increasing disorder level, it is more

plausibly attributed to impurity-induced states within the gap: for sign-changing order parameters, e.g., a two-band $s^{\pm}$ order parameter, a finite γ_0 at zero field and a linear temperature dependence of C/T at low T—as observed in YFe_2Ge_2 (Fig. 3)—are expected when the level of impurity scattering increases above a critical threshold [32]. The field dependence of γ_0 is also consistent with this scenario [33,34], which is in line with earlier theoretical predictions [3] for YFe_2Ge_2.

All data needed to evaluate the conclusions in the paper are present in the paper, the Supplementary Materials, and the Data Repository at the University of Cambridge and can be downloaded from [35].

We thank, in particular, N. Halcovitch for assistance with single-crystal XRD, and A. Chubukov, C. Geibel, G. Lonzarich, J. Schmalian, F. Steglich, and M. Sutherland for helpful discussions. The work was supported by the EPSRC of the UK (Grants No. EP/K012894/1 and No. EP/P023290/1) and by Trinity College.

*Corresponding author.
jc732@cam.ac.uk
†Present address: Clarendon Laboratory, Department of Physics, University of Oxford, Oxford OX1 3PU, United Kingdom.

[1] Y. Zou, Z. Feng, P. W. Logg, J. Chen, G. Lampronti, and F. M. Grosche, Fermi liquid breakdown and evidence for superconductivity in YFe_2Ge_2, Phys. Status Solidi RRL **8**, 928 (2014).
[2] G. R. Stewart, Superconductivity in iron compounds, Rev. Mod. Phys. **83**, 1589 (2011).
[3] A. Subedi, Unconventional sign-changing superconductivity near quantum criticality in YFe_2Ge_2, Phys. Rev. B **89**, 024504 (2014).
[4] D. J. Singh, Superconductivity and magnetism in YFe_2Ge_2, Phys. Rev. B **89**, 024505 (2014).
[5] M. Avila, S. Bud'ko, and P. Canfield, Anisotropic magnetization, specific heat and resistivity of RFe_2Ge_2 single crystals, J. Magn. Magn. Mater. **270**, 51 (2004).
[6] F. Hardy, R. Eder, M. Jackson, D. Aoki, C. Paulsen, T. Wolf, P. Burger, A. Böhmer, P. Schweiss, P. Adelmann, R. A. Fisher, and C. Meingast, Multiband superconductivity in KFe_2As_2: Evidence for one isotropic and several Liliputian energy gaps, J. Phys. Soc. Jpn. **83**, 014711 (2014).
[7] S. Khim, S. Aswartham, V. Grinenko, D. Efremov, C. G. Blum, F. Steckel, D. Gruner, A. U. Wolter, S. L. Drechsler, C. Heß, S. Wurmehl, and B. Büchner, A calorimetric investigation of $RbFe_2As_2$ single crystals, Phys. Status Solidi B **254**, 1600208 (2017).
[8] A. F. Wang, B. Y. Pan, X. G. Luo, F. Chen, Y. J. Yan, J. J. Ying, G. J. Ye, P. Cheng, X. C. Hong, S. Y. Li, and X. H. Chen, Calorimetric study of single-crystal $CsFe_2As_2$, Phys. Rev. B **87**, 214509 (2013).
[9] Q. Si, R. Yu, and E. Abrahams, High-temperature superconductivity in iron pnictides and chalcogenides, Nat. Rev. Mater. **1**, 16017 (2016).
[10] J. P. Reid *et al.*, From *d*-wave to *s*-wave pairing in the iron-pnictide superconductor $(Ba,K)Fe_2As_2$, Supercond. Sci. Technol. **25**, 084013 (2012).
[11] F. Hardy, A. E. Böhmer, D. Aoki, P. Burger, T. Wolf, P. Schweiss, R. Heid, P. Adelmann, Y. X. Yao, G. Kotliar, J. Schmalian, and C. Meingast, Evidence of Strong Correlations and Coherence-Incoherence Crossover in the Iron Pnictide Superconductor KFe_2As_2, Phys. Rev. Lett. **111**, 027002 (2013).
[12] Y. P. Wu, D. Zhao, A. F. Wang, N. Z. Wang, Z. J. Xiang, X. G. Luo, T. Wu, and X. H. Chen, Emergent Kondo Lattice Behavior in Iron-Based Superconductors AFe_2As_2 (A = K, Rb, Cs), Phys. Rev. Lett. **116**, 147001 (2016).
[13] D. Zhao, H. L. Wo, J. Li, D. W. Song, L. X. Zheng, S. J. Li, L. P. Nie, X. G. Luo, J. Zhao, T. Wu, and X. H. Chen, Approaching itinerant magnetic quantum criticality through a Hund's coupling induced electronic crossover in the YFe_2Ge_2 superconductor, Phys. Rev. B **101**, 064511 (2020).
[14] A. Georges, L. de' Medici, and J. Mravlje, Strong correlations from Hund's coupling, Annu. Rev. Condens. Matter Phys. **4**, 137 (2013).
[15] I. Felner, B. Lv, K. Zhao, and C. W. Chu, High-pressure resistivity of YFe_2Si_2 and magnetic studies of $Y_{1-y}Ho_yFe_2Si_2$ and $YFe_2(Si_{1-x}Ge_x)_2$ systems, J. Supercond. Novel Magn. **28**, 1207 (2015).
[16] H. Kim, S. Ran, E. Mun, H. Hodovanets, M. Tanatar, R. Prozorov, S. Bud'ko, and P. Canfield, Crystal growth and annealing study of fragile, non-bulk superconductivity in YFe_2Ge_2, Philos. Mag. **95**, 804 (2015).
[17] J. Chen, K. Semeniuk, Z. Feng, P. Reiss, P. Brown, Y. Zou, P. W. Logg, G. I. Lampronti, and F. M. Grosche, Unconventional Superconductivity in the Layered Iron Germanide YFe_2Ge_2, Phys. Rev. Lett. **116**, 127001 (2016).
[18] J. Chen, M. B. Gamża, K. Semeniuk, and F. M. Grosche, Composition dependence of bulk superconductivity in YFe_2Ge_2, Phys. Rev. B **99**, 020501(R) (2019).
[19] P. C. Canfield and Z. Fisk, Growth of single crystals from metallic fluxes, Philos. Mag. B **65**, 1117 (1992).
[20] See Supplemental Material, which includes Refs. [16, 18,21–25], at http://link.aps.org/supplemental/10.1103/PhysRevLett.125.237002 for further details of crystal growth protocols, of single-crystal XRD refinement results and of the analysis of nuclear contribution to specific heat in the LT-A sample.
[21] B. H. Toby and R. B. Von Dreele, GSAS-II: The genesis of a modern open-source all purpose crystallography software package, J. Appl. Crystallogr. **46**, 544 (2013).
[22] G. Venturini and B. Malaman, X-ray single crystal refinements on some RT_2Ge_2 compounds (R = Ca, Y, La, Nd, U; T = Mn – Cu, Ru-Pd): Evolution of the chemical bonds, J. Alloys Compd. **235**, 201 (1996).
[23] J. Emsley, *The Elements* (Oxford University Press, Oxford, 1991).
[24] *SCALE3 ABSPACK—An Oxford Diffraction Program (1.0.4, gui: 1.0.3)* (Oxford Diffraction Ltd., Abingdon, UK, 2005).
[25] P. J. Becker and P. Coppens, Extinction within the limit of validity of the Darwin transfer equations. I. General formalism for primary and secondary extinction and their applications to spherical crystals, Acta Crystallogr. Sect. A **30**, 129 (1974).

[26] J.-Q. Yan, B. C. Sales, M. A. Susner, and M. A. McGuire, Flux growth in a horizontal configuration: An analog to vapor transport growth, Phys. Rev. Mater. **1**, 023402 (2017).

[27] H. Wilhelm, T. Lühmann, T. Rus, and F. Steglich, A compensated heat-pulse calorimeter for low temperatures, Rev. Sci. Instrum. **75**, 2700 (2004).

[28] E. Vincent, J. Hammann, L. Taillefer, K. Behnia, N. Keller, and J. Flouquet, Low-field diamagnetic response of the superconducting phases in UPt_3, J. Phys. Condens. Matter **3**, 3517 (1991).

[29] J. S. Kim, B. D. Faeth, Y. Wang, P. J. Hirschfeld, G. R. Stewart, K. Gofryk, F. Ronning, A. S. Sefat, K. Y. Choi, and K. H. Kim, Specific heat to H_{c2}: Evidence for nodes or deep minima in the superconducting gap of underdoped and overdoped $Ba(Fe_{1-x}Co_x)_2As_2$, Phys. Rev. B **86**, 014513 (2012).

[30] A. A. Abrikosov and L. P. Gor'kov, Contribution to the theory of superconducting alloys with paramagnetic impurities, Sov. Phys JETP **12**, 1243 (1961).

[31] K. Okazaki *et al.*, Octet-line node structure of superconducting order parameter in KFe_2As_2, Science **337**, 1314 (2012).

[32] Y. Bang and G. R. Stewart, Superconducting properties of the $s^{\pm}$-wave state: Fe-based superconductors, J. Phys. Condens. Matter **29**, 123003 (2017).

[33] Y. Bang, Volovik Effect in the $\pm$s-Wave State for the Iron-Based Superconductors, Phys. Rev. Lett. **104**, 217001 (2010).

[34] Y. Wang, J. S. Kim, G. R. Stewart, P. J. Hirschfeld, S. Graser, S. Kasahara, T. Terashima, Y. Matsuda, T. Shibauchi, and I. Vekhter, Volovik effect in a highly anisotropic multiband superconductor: Experiment and theory, Phys. Rev. B **84**, 184524 (2011).

[35] https://doi.org/10.17863/CAM.59394.